Near-field imaging of optical antenna modes in the mid-infrared

Robert L. Olmon[1,2], Peter M. Krenz[3], Andrew C. Jones[1], Glenn D. Boreman[3], Markus B. Raschke[1,†]

[1]*Department of Chemistry, University of Washington, Seattle, WA 98195*
[2]*Department of Electrical Engineering, University of Washington, Seattle, WA 98195*
[3]*Center for Research and Education in Optics and Lasers (CREOL), University of Central Florida, Orlando, FL 32816*
raschke@chem.washington.edu

Abstract: Optical antennas can enhance the coupling between free-space propagating light and the localized excitation of nanoscopic light emitters or receivers, thus forming the basis of many nanophotonic applications. Their functionality relies on an understanding of the relationship between the geometric parameters and the resulting near-field antenna modes. Using scattering-type scanning near-field optical microscopy (*s*-SNOM) with interferometric homodyne detection, we investigate the resonances of linear Au wire antennas designed for the mid-IR by probing specific vector near-field components. A simple effective wavelength scaling is observed for single wires with $\lambda_{\text{eff}} = \lambda/(2.0 \pm 0.2)$, specific to the geometric and material parameters used. The disruption of the coherent current oscillation by introducing a gap gives rise to an effective multipolar mode for the two near-field coupled segments. Using antenna theory and numerical electrodynamics simulations two distinct coupling regimes are considered that scale with gap width or reactive near-field decay length, respectively. The results emphasize the distinct antenna behavior at optical frequencies compared to impedance matched radio frequency (RF) antennas and provide experimental confirmation of theoretically predicted scaling laws at optical frequencies.

OCIS codes: (260.3910) Metal optics; (260.5740) Resonance; (310.6628) Subwavelength structures; (180.4243) Near-field microscopy

References and links

1. T. H. Taminiau, F. D. Stefani, F. B. Segerink, and N. F. van Hulst, "Optical antennas direct single-molecule emission," Nat. Photonics **2**, 234–237 (2008).
2. V. Giannini and J. A. Sánchez-Gil, "Excitation and emission enhancement of single molecule fluorescence through multiple surface-plasmon resonances on metal trimer nanoantennas," Opt. Lett. **33**, 899–901 (2008).
3. T. H. Taminiau, R. J. Moerland, F. B. Segerink, L. Kuipers, and N. F. van Hulst, "Lambda/4 resonance of an optical monopole antenna probed by single molecule fluorescence," Nano. Lett. **7**, 28–33 (2007).
4. S. Kühn, U. Håkanson, L. Rogobete, and V. Sandoghdar, "Enhancement of single-molecule fluorescence using a gold nanoparticle as an optical nanoantenna," Phys. Rev. Lett. **97**, 017402–4 (2006).
5. J. Aizpurua, G. W. Bryant, L. J. Richter, F. J. García de Abajo, B. K. Kelley, and T. Mallouk, "Optical properties of coupled metallic nanorods for field-enhanced spectroscopy," Phys. Rev. B **71**, 235420 (2005).
6. P. Krenz, J. Alda, and G. Boreman, "Orthogonal infrared dipole antenna," Infrared Phys. Technol. **51**, 340–343 (2008).
7. C. Fumeaux, M. A. Gritz, I. Codreanu, W. L. Schaich, F. J. González, and G. D. Boreman, "Measurement of the resonant lengths of infrared dipole antennas," Infrared Phys. Technol. **41**, 271–281 (2000).

#101966 - $15.00 USD Received 24 Sep 2008; revised 10 Nov 2008; accepted 11 Nov 2008; published 24 Nov 2008

8. N. Yu, E. Cubukcu, L. Diehl, M. A. Belkin, K. B. Crozier, F. Capasso, D. Bour, S. Corzine, and G. Höfler, "Plasmonic quantum cascade laser antenna," Appl. Phys. Lett. **91**, 173113–3 (2007).
9. A. Cvitkovic, N. Ocelic, J. Aizpurua, R. Guckenberger, and R. Hillenbrand, "Infrared imaging of single nanoparticles via strong field enhancement in a scanning nanogap," Phys. Rev. Lett. **97**, 060801 (2006).
10. L. Tang, S. E. Kocabas, S. Latif, A. K. Okyay, D.-S. Ly-Gagnon, K. C. Saraswat, and D. A. B. Miller, "Nanometre-scale germanium photodetector enhanced by a near-infrared dipole antenna," Nat. Photonics **2**, 226–229 (2008).
11. M. Pelton, J. Aizpurua, and G. Bryant, "Metal-nanoparticle plasmonics," Laser Photon. Rev. **2**, 136–159 (2008).
12. J. N. Farahani, D. W. Pohl, H.-J. Eisler, and B. Hecht, "Single quantum dot coupled to a scanning optical antenna: A tunable superemitter," Phys. Rev. Lett. **95**, 017402–4 (2005).
13. S.-D. Liu, M.-T. Cheng, Z.-J. Yang, and Q.-Q. Wang, "Surface plasmon propagation in a pair of metal nanowires coupled to a nanosized optical emitter," Opt. Lett. **33**, 851–853 (2008).
14. In some applications, a low-frequency feed line may be used to extract an electrical signal from an optical antenna, see, e.g., F. J. González and G. D. Boreman, "Comparison of dipole, bowtie, spiral and log-periodic IR antennas," Infrared Phys. Technol. **46**, 418–428 (2005).
15. L. Novotny, "Effective wavelength scaling for optical antennas," Phys. Rev. Lett. **98**, 266802 (2007).
16. F. Neubrech, T. Kolb, R. Lovrincic, G. Fahsold, A. Pucci, J. Aizpurua, T. W. Cornelius, M. E. Toimil-Molares, R. Neumann, and S. Karim, "Resonances of individual metal nanowires in the infrared," Appl. Phys. Lett. **89**, 253104–3 (2006).
17. J. Merlein, M. Kahl, A. Zuschlag, A. Sell, A. Halm, J. Boneberg, P. Leiderer, A. Leitenstorfer, and R. Bratschitsch, "Nanomechanical control of an optical antenna," Nat. Photonics **2**, 230–233 (2008).
18. K. B. Crozier, A. Sundaramurthy, G. S. Kino, and C. F. Quate, "Optical antennas: Resonators for local field enhancement," J. Appl. Phys. **94**, 4632–4642 (2003).
19. P. Mühlschlegel, H.-J. Eisler, O. J. F. Martin, B. Hecht, and D. W. Pohl, "Resonant optical antennas," Science **308**, 1607 (2005).
20. O. L. Muskens, V. Giannini, J. A. Sánchez-Gil, and J. Gómez Rivas, "Optical scattering resonances of single and coupled dimer plasmonic nanoantennas," Opt. Express **15**, 17736–17746 (2007).
21. P. J. Schuck, D. P. Fromm, A. Sundaramurthy, G. S. Kino, and W. E. Moerner, "Improving the mismatch between light and nanoscale objects with gold bowtie nanoantennas," Phys. Rev. Lett. **94**, 017402–4, (2005).
22. G. W. Bryant, F. J. García de Abajo, and J. Aizpurua, "Mapping the plasmon resonances of metallic nanoantennas," Nano. Lett. **8**, 631–636 (2008).
23. H. Fischer and O. J. F. Martin, "Engineering the optical response ofplasmonic nanoantennas," Opt. Express **16**, 9144–9154 (2008).
24. B. P. Joshi and Q.-H. Wei, "Cavity resonances of metal-dielectric-metal nanoantennas," Opt. Express **16**, 10315–10322 (2008).
25. E. R. Encina and E. A. Coronado, "Resonance conditions for multipole plasmon excitations in noble metal nanorods," J. Phys. Chem. C **111**, 16796–16801 (2007).
26. F. Keilmann and R. Hillenbrand, "Near-field microscopy by elastic light scattering from a tip," Philos. Trans. R. Soc. London Ser. A **362**, 787–805 (2004).
27. K. G. Lee, H. W. Kihm, Kihm J. E., Choi W. J., Kim H., Ropers C., Park D. J., Yoon Y. C., Choi S. B., Woo D. H., Kim J., Lee B., Park Q. H., Lienau C., and Kim D. S, "Vector field microscopic imaging of light," Nature Photon. **1**, 53–56 (2007).
28. M. Rang, A. C. Jones, F. Zhou, Z.-Y. Li, B. J. Wiley, Y. Xia, and M. B. Raschke, "Optical near-field mapping of plasmonic nanoprisms," Nano. Lett. **8**, 3357–3363 (2008).
29. M. B. Raschke, L. Molina, T. Elsaesser, D. H. Kim, W. Knoll, and K. Hinrichs, "Apertureless near-field vibrational imaging of block-copolymer nanostructures with ultrahigh spatial resolution," Chem. PhysChem. **6**, 2197–2203 (2005).
30. Since the detected signal is a demodulation of the tip-sample dither frequency, it actually represents the near-field gradient within the dither region rather than just the near-field intensity.
31. L. Gomez, R. Bachelot, A. Bouhelier, G. P. Wiederrecht, S. H. Chang, S. K. Gray, F. Hua, S. Jeon, J. A. Rogers, M. E. Castro, S. Blaize, I. Stefanon, G. Lerondel, and P. Royer, "Apertureless scanning near-field optical microscopy: a comparison between homodyne and heterodyne approaches," J. Opt. Soc. Am. B **23**, 823–833 (2006).
32. T. Taubner, R. Hillenbrand, and F. Keilmann, "Performance of visible and mid-infrared scattering-type near-field optical microscopes," J. Microsc. **210**, 311–314 (2003).
33. In addition, a backscattered far-field background leads to a self-homodyne signal amplification with in general unspecified phase [34]. For weak sample scattering (this work) or strongly resonant (e.g., plasmonic) excitation [28], spatial phase variations of this background can be neglected resulting in a mere constant s-SNOM signal offset at constant phase.
34. M. B. Raschke and C. Lienau, "Apertureless near-field optical microscopy: Tip–sample coupling in elastic light scattering," Appl. Phys. Lett. **83**, 5089–5091 (2003).
35. For details on phase-resolved imaging of IR active nanostructures, see A. Jones, R. Olmon, S. Skrabalak, Y. Xia, and M. Raschke (in preparation).

#101966 - $15.00 USD Received 24 Sep 2008; revised 10 Nov 2008; accepted 11 Nov 2008; published 24 Nov 2008

36. C. Balanis, *Antenna Theory: Analysis and Design*. John Wiley & Sons, Inc., second edition, 1997.
37. W. L. Stutzman and G. A. Thiele, *Antenna Theory and Design*. John Wiley & Sons, Inc., second edition, 1981.
38. W. Rechberger, A. Hohenau, A. Leitner, J. R. Krenn, B. Lamprecht, and F. R. Aussenegg, "Optical properties of two interacting gold nanoparticles," Optics Communications **220**, 137–141 (2003).
39. S. J. Orfanidis, *Electromagnetic Waves and Antennas*. Online book, retrieved August 2008. `http://www.ece.rutgers.edu/~{}orfanidi/ewa/`.
40. G. V. Borgiotti, "A novel expression for the mutual admittance of planar radiating elements," IEEE Trans. Antennas Propag. **AP-16**, 329 (1968).
41. T. Søndergaard and S. I. Bozhevolnyi, "Strip and gap plasmon polariton optical resonators," Phys. Status Solidi B **245**, 9–19 (2008).
42. C. C. Neacsu, J. Dreyer, N. Behr, and M. B. Raschke, "Scanning-probe raman spectroscopy with single-molecule sensitivity," Phys. Rev. B **73**, 193406–4 (2006).
43. A. Hartschuh, E. J. Sánchez, X. S. Xie, and L. Novotny, "High-resolution near-field raman microscopy of single-walled carbon nanotubes," Phys. Rev. Lett. **90**, 095503 (2003).
44. R. Hillenbrand and F. Keilmann, "Optical oscillation modes of plasmon particles observed in direct space by phase-contrast near-field microscopy," Appl. Phys. B **73**, 239–243 (2001).
45. R. Ossikovski, Q. Nguyen, and G. Picardi, "Simple model for the polarization effects in tip-enhanced raman spectroscopy," Phys. Rev. B **75**, 045412 (2007).
46. R. Hillenbrand, private communication, July 2008.
47. A. Alù and N. Engheta, "Tuning the scattering response of optical nanoantennas with nanocircuit loads," Nature Photon. **2**, 307–310 (2008).
48. M. Sukharev and T. Seideman, "Phase and polarization control as a route to plasmonic nanodevices," Nano. Lett. **6**, 715–719 (2006).

1. Introduction

Expanding the realm of geometric optics, optical antennas provide a means of focusing radiant visible and infrared (IR) light down to nanometer length scales. This has potential for a wide range of novel photonic applications including chemical [1, 2, 3, 4, 5] and thermal sensors [6, 7], near-field microscopy [8, 9], nanoscale photodetectors [10], and plasmonic devices [11, 12, 13]. However, addressing the up to several orders of magnitude dimensional mismatch between the emitter or receiver in the form of molecules, quantum dots, or waveguides on the one hand, and the associated wavelengths of the radiation on the other has remained a primary challenge. With optical antennas, this challenge typically needs to be met by through-space near-field coupling and not by a feed line from the receiver or emitter as in the radio frequency (RF) case [14]. By interacting with nanoscale structures through the near-field, one may take advantage of spatial localization and field enhancement on length scales comparable to the size of the nanoscopic source. Therefore, in contrast to RF antenna designs, where the focus is on optimizing far-field characteristics in order to obtain better long distance transmission and reception performance, optical antenna designs must first emphasize the near-field behavior.

Like RF antennas, optical antennas are resonant structures responding to specific frequencies through both the geometrical and material characteristics of the antennas and their environments [16, 17, 18, 19, 15, 3, 20, 21]. However, at optical frequencies, different scaling laws arise associated with the finite skin depth and corresponding resistive losses, finite aspect ratios and an inhomogeneous dielectric environment. Far-field spectral studies [16, 17, 21, 19, 20, 18] and theoretical modeling [22, 23, 24, 25] have already addressed several fundamental aspects of optical antennas. Yet, the general understanding of the material and geometrical basis of optical antenna modes is still incomplete. In order to gain insight into the near-field antenna modes and their geometric scaling, we measured the evanescent near-field distribution in the form of selected vector-field components of linear IR antennas using scattering-type scanning near-field optical microscopy (*s*-SNOM) [26, 27]. The linear wire antenna was chosen as the simplest implementation of an optical antenna to investigate the fundamentals of length scaling and the effect of coupling between adjacent antenna segments. The antennas are designed for the mid-IR spectral region due to the comparable ease of structure fabrication as compared to

#101966 - $15.00 USD Received 24 Sep 2008; revised 10 Nov 2008; accepted 11 Nov 2008; published 24 Nov 2008

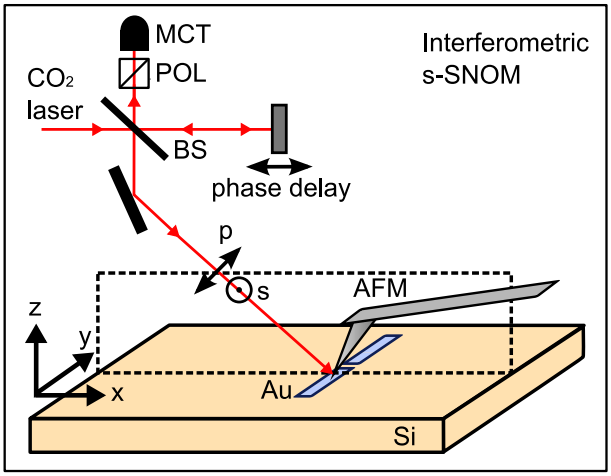

Fig. 1. Scattering-type scanning near-field optical microscope (*s*-SNOM) with interferometric homodyne detection to probe specific near-field vector components of optical antennas.

the visible spectral range. In addition, IR optical antennas are in great technological need with many potential applications in chemical spectroscopy, ultrafast IR and THz transient detection, and remote sensing. [10, 6, 7, 8, 9, 16, 25, 5].

2. Experiment and Theory

Au wire antennas were fabricated by electron beam lithography onto native oxide covered Si wafers (resistivity $\rho = 3-6\,\mathrm{k}\Omega\cdot\mathrm{cm}$). The wafers were metalized with a 5 nm seed layer of Ti and 70–80 nm of Au to produce wires approximately 120–150 nm in width, with lengths ranging from 1.6 μm to 7.0 μm, with and without center gaps ranging from 50 nm to 200 nm in width. All structures were separated from each other by 20 μm to ensure mutual decoupling and to minimize extraneous backscattering within the illuminating focal area.

The *s*-SNOM setup is based on a modified atomic force microscope (AFM, CP-Research, Veeco Inc.) operating in non-contact mode as shown in Fig. 1 and discussed in Ref. [28, 29]. Pt tips were used in the measurements shown (Si tips were used as well with similar results, though with lower scattering intensities). Both tips exhibit weak dipole-dipole tip-sample coupling, and thus minimize perturbation of the intrinsic field distribution [28]. Excitation is provided by a CO_2 laser ($\lambda = 10.6$ μm) incident onto the sample via a Cassegrain objective (NA = 0.5) at a 70° angle with respect to the surface normal. The elliptical focus has a width at the sample of $\sim$13 μm. Polarization selective excitation and tip-scattered near-field detection is performed with p- and s-polarized light defined with respect to the incidence plane. For excitation, the incident polarization was chosen along the antenna axis. The tip-scattered light is detected using a mercury-cadmium-telluride (MCT) photodetector. The optical signal is recorded while raster scanning the sample and is typically demodulated at the second-harmonic of the tip-dither frequency [30]. Homodyne amplification was performed to extract phase information from the optical near-field signal [31, 32]. To first order, given the scattered near-field E_{nf} and the reference field E_{ref} with corresponding phases ϕ_{nf} and ϕ_{ref}, the detected intensity $I \approx |E_{nf}|^2 + |E_{ref}|^2 + 2|E_{nf}\cdot E_{ref}|\cos\Phi$, with $\Phi = \phi_{nf} - \phi_{ref}$ [33]. The in-plane E_y and out-of-plane E_z near-field vector components can be extracted by selective amplification of the respective polarization components by appropriately adjusting the magnitude of the reference

#101966 - $15.00 USD Received 24 Sep 2008; revised 10 Nov 2008; accepted 11 Nov 2008; published 24 Nov 2008

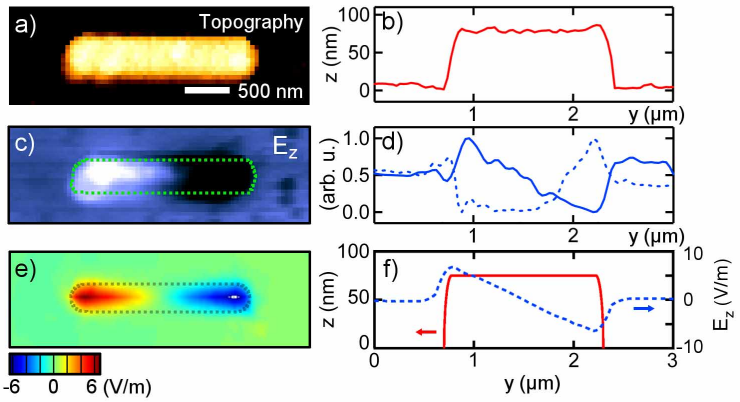

Fig. 2. Topography (a) for a $L = 1.6\,\mu$m linear IR dipole antenna and E_z *s*-SNOM near-field image (c), with corresponding line scans (b) and (d). *s*-SNOM contrast (c) is due to selective phase amplification as seen in the two 180° out of phase line scans (solid vs. dashed line in (d)). Corresponding simulated in-plane (e) and cross sectional (f) E_z distribution for a half-cylinder model antenna geometry. Dashed lines in (c) and (e) demarcate the topography.

signal [35].

Electrodynamics simulations were performed using HFSS (Ansoft Corp.) which uses a full-wave finite element method to evaluate the electromagnetic fields of selected model geometries. To simulate the experiment, the antennas are excited by a 10.6 μm plane wave with a strength of 1 V/m and with an incident angle of 70° with respect to the surface normal. The dielectric constants of Si and Au used are $\varepsilon_{\mathrm{Si}} = 11.7 + i1.52\mathrm{x}10^{-5}$ and $\varepsilon_{\mathrm{Au}} = -4790 + i4270$, respectively, as measured by infrared ellipsometry of the Si substrates and of thin Au films fabricated under the same conditions as the antennas. The wires were modeled as Au half-cylinders terminated by quarter spheres to approximate the shape of the antennas and minimize numerical artifacts compared to rectangular cross sections.

3. Results and discussion

Probing the out-of-plane E_z field component is ideally suited for identifying the antenna modes due to the anti-phase oscillations associated with each electromagnetic pole (*i.e.* charge center). In addition, an enhanced scattering for p-polarization due to the tip geometry benefits the *s*-SNOM sensitivity. Figure 2 shows the simultaneously recorded topography (a) and (b) and *s*-SNOM signal for the E_z near-field component (c) and (d) as probed under the $\mathrm{s_{in}p_{out}}$ polarization combination of a single Au wire of length $L = 1.6\,\mu$m. The optical contrast (c) is due to the respective constructive and destructive interference of the antenna near-field with the interferometer reference field [28]. The apparent out of phase oscillations of the E_z field across the wire signifies dipolar behavior. Depending on the phase delay of the interferometer the contrast inverts as shown, *e.g.*, in line traces for a 180° reference phase reversal (solid vs. dashed line in Fig. 2(d)). For comparison, Figs. 2(e) and 2(f) show the corresponding simulated monomer field for $L = 1.6\,\mu$m, 20 nm above the metal in-plane and cross-sectioned, respectively. The highest field strength is located near the wire ends with a near-linear variation across the wire, in excellent agreement with the experimental observation.

The half-wavelength dipole resonance antenna length for incident excitation of 10.6 μm as determined from the numerical simulations is $L = (2.6 \pm 0.2)\,\mu$m, implying an effec-

#101966 - $15.00 USD Received 24 Sep 2008; revised 10 Nov 2008; accepted 11 Nov 2008; published 24 Nov 2008

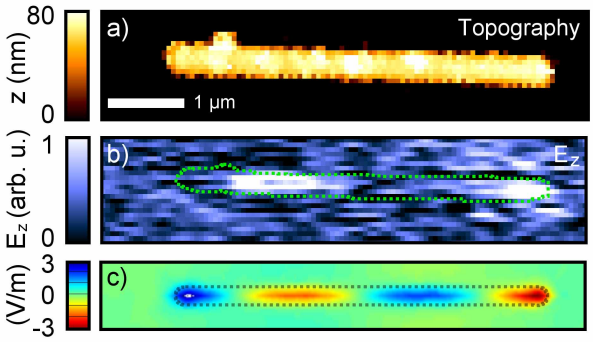

Fig. 3. Topography (a) and E_z *s*-SNOM signal (b) for a $L = 5.0\,\mu$m antenna showing the first higher order mode corresponding to $L \approx \lambda_{\text{eff}}$. The resulting quadrupole oscillation is reproduced in the corresponding E_z-field simulation (c) showing enhanced field strength at the wire ends.

tive wavelength of approximately $\lambda_{\text{eff}} = (5.2 \pm 0.4)\,\mu$m corresponding to a scaling factor of $\lambda/\lambda_{\text{eff}} = 2.0 \pm 0.2$ for the geometric and material parameters used. To arrive at this value, the input impedances for a series of center-fed antennas with lengths ranging from 2.0 μm to 5.0 μm were computed with a step size of 10 nm. Antenna resonance then corresponds to an input reactance of $X = 0\,\Omega$. The resonant length of $\sim 2.6\,\mu$m is found to be in good agreement with results obtained for related geometries studied [16, 18].

This value can also be compared with an analytic scaling approximation [15] using an effective homogeneous dielectric constant for the surrounding medium of the antenna. Assuming an arithmetic mean of the dielectric constants of Si and air ($(\varepsilon_{Si} + \varepsilon_{air})/2 = 6.35$) results in an effective wavelength of $\sim 3.6\,\mu$m. Considering the geometric mean ($\sqrt{\varepsilon_{Si}\varepsilon_{air}} = 3.42$), the effective wavelength is $\sim 5.1\,\mu$m, a value close to the numerical results above.

These effective wavelengths are considerably reduced compared to the free space wavelength of $10.6\,\mu$m. The difference can be attributed to the observations made previously, noting that the resonance wavelength is reduced due to the ohmic loss in the metal at optical frequencies, the dielectric properties of the substrate, and the finite antenna width [15, 7, 16, 18].

A dipole behavior for single wires can still be discerned in *s*-SNOM measurements of Au wires with lengths greater than the dipole resonance length. However, an increasingly asymmetrically distorted E_z distribution results, as has been seen in measurements for antennas of lengths up to 3.4 μm (data not shown), which is the longest measured structure still supporting a dipole-like field distribution. If the length of the antenna is extended further, multiple half-wavelength current oscillations develop on the antenna for a given excitation frequency with resonances $L \approx n \times \lambda_{\text{eff}}/2$ with $n = 1, 2...$ [36]. The first higher order mode ($n = 2$) corresponding to the $L \approx \lambda_{\text{eff}}$ resonance is seen in Fig. 3 for a wire of length $L = 5.0$ μm, corresponding to the theoretically predicted mode at $\lambda_{\text{eff}} = (5.2 \pm 0.4)\,\mu$m as discussed above. The two-fold maxima and minima observed for the E_z field represent a quadrupole excitation as also seen in corresponding numerical simulations for the same geometry (c). The smaller spatial extent and higher strength of the fields at the wire endpoints, as observed in the experiment, are characteristic for this excitation mode and are also reproduced theoretically.

In classical antenna theory the occurrence of these antenna resonances depends on the input impedance at the feed point. Considering the entire transceiver system, including the signal source or receiver, transmission lines, and the antenna, resonance is achieved when the antenna presents a conjugate input reactance, which ensures maximum power transfer [37]. The sig-

#101966 - $15.00 USD Received 24 Sep 2008; revised 10 Nov 2008; accepted 11 Nov 2008; published 24 Nov 2008

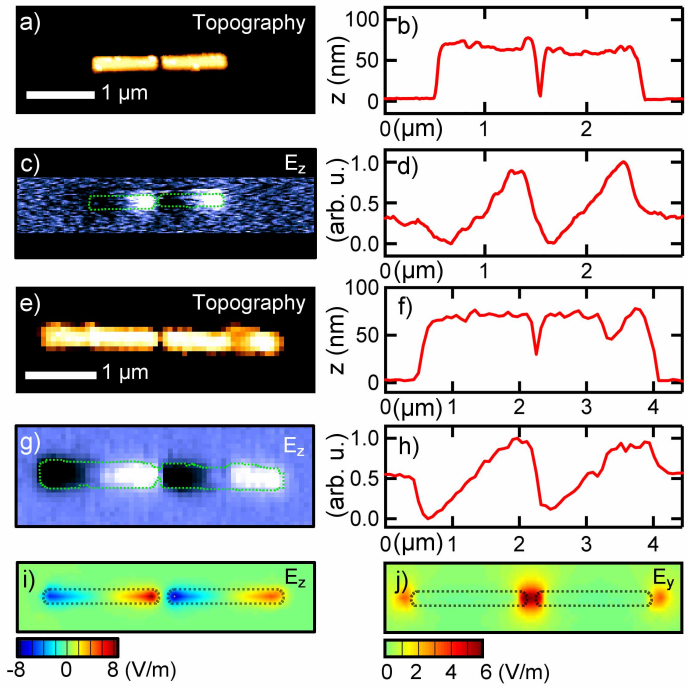

Fig. 4. Topography (a) and (b) and E_z *s*-SNOM signal (c) and (d) for a structure of overall length $L = 2.0\,\mu$m with a gap width of 150 nm and corresponding results for a similar geometry of length $L = 3.4\,\mu$m (e)–(h). Introducing the gap gives rise to a disruption of the original dipole resonance and a splitting into two coupled individual dipole modes. Numerical simulations for expected field distributions for E_z (i) and E_y (j).

nificance of the $\lambda/2$ antenna length is merely that such an antenna presents nearly zero input reactance and approximately $75\,\Omega$ input resistance intrinsically, and thus can be made to resonate easily, and radiate efficiently [36]. However, in the optical regime the currents on the two arms of a dimer antenna structure do not interact in the same manner as in the RF. Consequently, introducing a so-called "feed gap" into the center of an equivalent half-wave linear optical antenna is inapplicable in attaining antenna resonance [15].

This is shown in Fig. 4 displaying the topographies and near-field E_z distributions for antenna structures of overall length $L = 2.0\ \mu$m (a)–(d) and $L = 3.4\ \mu$m (e)–(h) after introducing gaps of 150 nm (with similar results also observed for 100 nm and 40 nm gaps). As is evident from the observed field distributions, the antenna current oscillations no longer represent single dipole excitations as was observed for individual wires of corresponding length. Instead, a dipole behavior is seen for each of the segments, making the overall optical near-field distribution reminiscent to that of a linear quadrupole. This is reflected in corresponding numerical simulations for the $L = 3.4\ \mu$m antenna dimer with a gap of 150 nm (i).

The resulting antenna resonance can be described by two separate, albeit coupled, dipole antennas. In order to analyze the coupling and its effect on the antenna resonance, given the linear wire antenna geometry, simple classical RF antenna coupling theory can be adopted. The mutual interaction of the respective antenna electric fields with the underlying currents of

#101966 - $15.00 USD Received 24 Sep 2008; revised 10 Nov 2008; accepted 11 Nov 2008; published 24 Nov 2008

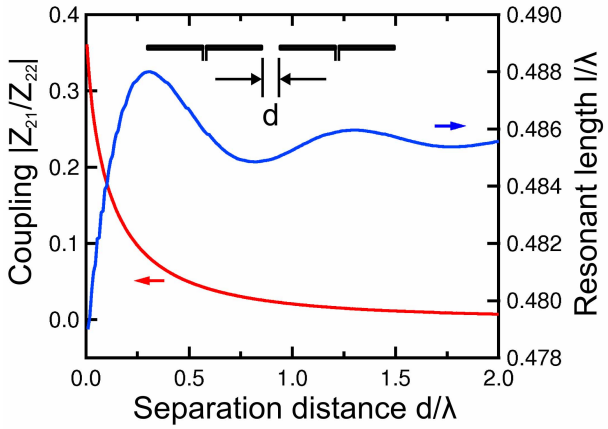

Fig. 5. Coupling of two equal-length ideal half-wave coaxial dipole antennas separated by distance d relative to the wavelength. The coupling is manifested in a change in mutual impedance $|Z_{21}/Z_{22}|$ (here normalized by the self-impedance at the input) with decreased separation distance. The associated oscillatory variations in resonant length converge to the length of a single resonant dipole.

neighboring antennas is described by their mutual impedance [36]. For two identical coaxial antennas of length l separated by a gap of size d, in the approximation of negligible width of the antenna segments, assuming a free space environment, and a sinusoidal current, the mutual impedance Z_{21} referred to the input terminals (*i.e.* the impedance change occurring at the input of antenna 2 due to the electric field radiated by antenna 1) is given by [39]

$$Z_{21} = \frac{i\sqrt{\mu_0/\varepsilon_0}}{4\pi \sin^2(kh)} \int_{-h}^{h} F(z)dz, \tag{1}$$

where $h = l/2$, μ_0 is the vacuum magnetic permeability, ε_0 is the electric permittivity, k is the wavenumber of the driving field, and

$$F(z) = \left[\frac{e^{-ik(R-h)}}{R-h} + \frac{e^{-ik(R+h)}}{R+h} - 2\cos(kh)\frac{e^{-ikR}}{R} \right] \sin[k(h-|z|)], \tag{2}$$

with $R = z + l + d$. While a single antenna is subject to self-impedance only (Z_{11} or Z_{22}), two antennas undergo a shift in total impedance equal to the sum of the self impedance and the mutual impedance scaled by the antenna current ratio: $Z_2 = Z_{22} + Z_{21}(I_1/I_2)$, where I_j denotes current in wire j. Figure 5 shows the resulting coupling observed as an increased mutual impedance (shown here normalized to the self impedance, *i.e.* $|Z_{21}/Z_{22}|$), for a pair of collinear ideal half-wave antennas as a function of gap width.

Since resonance in RF antennas is dependent on the input impedance of the antenna, coupling is associated with resonance shifts. This effect is seen when one compares the resonant lengths (reactance $X = 0\ \Omega$) of antennas as a function of separation distance as seen in Fig. 5. The result is a characteristic, though small, oscillation in resonant length converging to that of a single resonant dipole antenna with length $L = 0.4857\lambda$ for large separation distances. This oscillatory behavior is an interference effect. Considering the 90° phase difference between antenna current and the radiated field, for separation distances of $(n+1/4)\lambda$ (for $n = 0, 1, 2, \cdots$),

#101966 - $15.00 USD Received 24 Sep 2008; revised 10 Nov 2008; accepted 11 Nov 2008; published 24 Nov 2008

the current in each antenna is in phase with the electric field radiated by the other antenna, and they interact constructively. Conversely, when the antennas are separated by $(n+3/4)\lambda$, the currents are out of phase with the radiated fields. Both situations lead to a change in input impedance which require the antenna length to increase for constructive and decrease for destructive interference, respectively, in order to achieve resonance. The sharp drop in resonance length at small separation distances can be attributed to a reactive near-field interaction, which dominates for distances of $r < 0.62\sqrt{L^3/\lambda}$ [36]. The mutual impedance effect is particularly strong when the antennas are oriented side by side, with each antenna located in the direction of maximum radiation of the other. In that case, the mutual impedance significantly exceeds that of the collinear case [36, 39, 40].

Applying this analysis for the optical regime, both the effective wavelength and changes in the emitted field distribution due to the inhomogeneous dielectric environment and finite aspect ratio of the antennas have to be considered. Nevertheless, the fundamental coupling mechanism in the form of the field retardation effects is expected to prevail. This is supported by previous experiments that indicate similar coupling behavior for antennas in the visible and near-IR [5]. Therefore, this reactive coupling in the coaxial antenna geometry as determined by the wavelength and the antenna size has only a small effect on the resonance length of the individual antenna segments. The effective scaling as established for single wires is also directly applicable for the individual segments of the coupled dimer antennas.

In addition to this long range interaction a local interaction on much shorter distances occurs which amounts to an increase in enhancement with decreasing distance [21]. Its magnitude, however, depends sensitively on the local geometric details at the gap, and to first order, is expected to scale with gap width as the radius of the antenna ends. This can give rise to substantial enhancement values, especially for distances in the range of just several nanometers for corresponding apex radii as shown in the visible spectral range for collinear wires [19, 5, 24, 41] and bow-tie antennas [21]. Such a geometric dependence is reminiscent of tip-enhanced spectroscopy where a tip-distance dependence of the enhancement in the gap has been established to scale with the radius of the tip apex [34, 42, 43].

This local coupling is expected to manifest itself largely in a distance dependent variation of the E_y field for our geometries as seen in the calculated field distribution in Fig. 4(j). While the strength of the E_z field at the ends dominates over the E_y amplitude in general, E_y in the gap increases rapidly and becomes dominant for gap widths < 200 nm. In contrast, the phase change of the E_z field across the gap gives rise to $E_z = 0$ at its center. Hence, enhancement of E_z is spatially less localized and experiences a comparatively small variation as a function of gap width.

While both the E_z and E_y components hold much promise in controlling light at these subwavelength dimensions as determined by the gap width, the enhancement of the E_y component in particular is key for field-enhanced spectroscopies [5, 2], subwavelength emitters [8], and nanometer-scale photodetection [10]. The corresponding experimental observation of this in-plane field component, however, has remained a major challenge [8, 44]. The experimental difficulties arise due to the relative insensitivity of the tip for scattering s-polarized field components. Further, due to the finite taper angle of the tip, depolarization of the dominant p-polarized E_z signal contribution during the scattering process is a concern [45]. This, together with all E_y components across the antenna being in phase, makes assignment of the *s*-SNOM signal difficult. In $s_{in}s_{out}$ experiments (see Appendix), contrast is observed with in-phase signal characteristics that would, in principle, be consistent with an E_y assignment. The results, however, have been inconclusive, with no signal observed in the gap or beyond the antenna endpoints. We attribute this to the antenna effect of the tip itself. For long wavelengths the scattering of the tip apex for s-polarization becomes increasingly inefficient compared to that for

#101966 - $15.00 USD Received 24 Sep 2008; revised 10 Nov 2008; accepted 11 Nov 2008; published 24 Nov 2008

longitudinal p-polarized excitation. This is in contrast to our related experiments for plasmonic nanoparticles in the visible where the E_y component could be identified [28].

Probing a gap field has been reported in recent IR studies of resonant antennas with gaps as large as 100 nm fabricated on the facet of a quantum cascade laser (QCL) [8]. In these studies, signals from the gap region as well as from the apex of the outer wire ends dominate the optical response, possibly due to the E_y field. However, no polarization sensitive detection is discussed. Also, despite the expected enhanced tip-scattering sensitivity for polarization parallel with respect to the tip axis, as stated by the authors, no signature of the characteristic E_z fields above the metal wires is detected. It is interesting to note that in recent independent IR experiments in other groups for antenna structures and gap widths with geometries similar to those discussed here, no significant gap fields could be observed [46].

4. Conclusion

In summary, we have demonstrated selective E_z vector-field probing in the IR at 10.6 μm to obtain modal information of optical wire antennas of various lengths. With an effective wavelength of $\lambda_{\text{eff}} = (5.2 \pm 0.4)\,\mu$m, scaling the monomer lengths beyond the half-wavelength dipole resonance of $\lambda_{\text{eff}}/2 = (2.6 \pm 0.2)\,\mu$m, the transition from a dipole to a quadrupole field distribution for a $L = 5.0\,\mu$m monomer was observed. In contrast, the dimers with the individual segments optically coupled across a small gap were revealed to have a new resonant behavior emerging from a superposition of individual monomer modes, reminiscent of a linear quadrupole, confirming theoretical predictions. Two manifestations of the coupling could be identified from the combined experimental, numerical, and analytical antenna theory analysis: resonant effects due to the current-field interaction as determined by the antenna separation distance and λ_{eff}, and local field enhancement effects determined by separation distances on a length scale of tens of nm. These results for linear antennas are fundamental and shall be applicable in general to other antenna geometries and wavelengths. They provide design criteria for more complex architectures to optimize the resonant interaction of both incident light with receptive devices and the near-field coupling to emissive particles. Further developments in, *e.g.*, impedance matching techniques for optical antennas [47] and in methods for spatial, temporal, and spectral control of light [48] will enhance the performance of future device applications including detectors at the nanoscale, chemical spectroscopy and thermal sensing.

Acknowledgments

The authors thank Rainer Hillenbrand, Lukas Novotny, Ralf Vogelgesang, Mikhail Belkin and Brian Lail for valuable discussions. We are indebted to Matthias Rang for indispensable experimental support. Funding from the National Science Foundation (NSF CAREER grant CHE 0748226) and support from the Environmental Molecular Sciences Laboratory at Pacific Northwest National Laboratory is greatly acknowledged.

Appendix

Here, we provide further details regarding imaging the in-plane E_y vector-field components of linear IR antennas. We have shown the capability of the *s*-SNOM setup to detect in-plane visible light from plasmonic nanoparticles under otherwise identical experimental conditions [28]. Similarly, in the present work experiments were aimed at imaging under $s_{in}s_{out}$ polarization configurations to detect the E_y component for the linear antennas in the IR. However, with the *s*-SNOM tip preferentially scattering p-polarized light, detection of s-polarized light is difficult in general. In Fig. 6, the simultaneously recorded topography (a) and corresponding *s*-SNOM signal (b) for the measured E_y near-field component of the $L = 1.6\,\mu$m monomer are shown

#101966 - $15.00 USD Received 24 Sep 2008; revised 10 Nov 2008; accepted 11 Nov 2008; published 24 Nov 2008

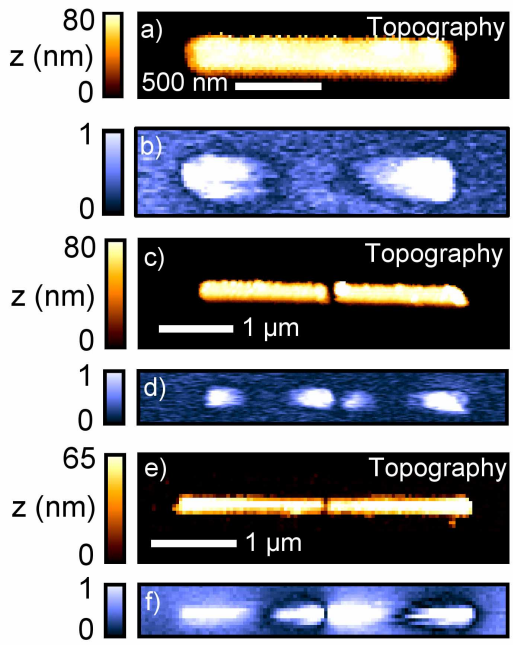

Fig. 6. The *s*-SNOM E_y field component imaged above a monomer antenna of length $L = 1.6\,\mu$m (a) and (b). Corresponding dimer fields for lengths $L = 3.35\,\mu$m and gap widths of 200 μm (c) and (d) and 50 μm (e) and (f). The in-phase nature of the field on the metal is predicted by theory, but off the metal, no field is seen in the gap or beyond the antenna ends contrary to theory due to preferential E_z scattering and tip depolarization effects.

together with the same field for the dimer geometries with overall lengths $L = 3.4\,\mu$m and gap widths 150 nm (c, d) and 40 nm (e, f). All structures exhibit E_z components as shown in Fig. 2(c) and Figs. 4(c) and 4(g). This has been observed using both Pt as well as Si as the tip material.

The phase behavior, showing in-phase emission for all poles both for the monomer as well as for the dimers would be consistent with the expected tip-scattered emission due to the E_y field component. However, the relative strength of the measured field and its spatial distribution compared to that of the simulated field (see, *e.g.*, Fig. 4(j)) suggest that the signal observed is dominated by a depolarized E_z component.

The absence of any field detected within the gap is notable. Yet, the strong, unambiguous E_z optical contrast observed and the near perfect agreement with theory suggest that the corresponding E_y field should exist. As already indicated in the manuscript, one possible reason for the apparent absence of a gap field is the antenna effect of the tip itself. Compared to the visible, as the wavelength of the light extends to the mid-IR, the dimensional mismatch between the tip apex and the wavelength increases. This leads to a decrease in scattering efficiency of the tip apex as the active scattering probe region for s-polarized light compared to p-polarized light. The result is a general insensitivity of *s*-SNOM using conventional tip geometries for IR fields polarized perpendicular to the tip apex.

#101966 - $15.00 USD Received 24 Sep 2008; revised 10 Nov 2008; accepted 11 Nov 2008; published 24 Nov 2008